Simulation of Incompressible Elastic Material Using Zonal Volume Constraints

by

Seung Heon Sheen

B.S., Texas A&M University, 2017

A THESIS SUBMITTED IN PARTIAL FULFILLMENT
OF THE REQUIREMENTS FOR THE DEGREE OF

Master of Science

in

THE FACULTY OF GRADUATE AND POSTDOCTORAL
STUDIES
(Computer Science)

The University of British Columbia
(Vancouver)

October 2020

The following individuals certify that they have read, and recommend to the Faculty of Graduate and Postdoctoral Studies for acceptance, the thesis entitled:

Simulation of Incompressible Elastic Material Using Zonal Volume Constraints

submitted by **Seung Heon Sheen** in partial fulfillment of the requirements for the degree of **Master of Science** in **Computer Science**.

Examining Committee:

Dinesh K. Pai, Computer Science
Supervisor

Uri M. Ascher, Computer Science
Examining Committee

Abstract

Simulation of human soft tissues in contact with their environment is essential in many fields, including visual effects and apparel design. Biological tissues are nearly incompressible. However, standard methods employ compressible elasticity models and achieve incompressibility indirectly by setting Poisson's ratio to be close to 0.5. This approach can produce results that are plausible qualitatively but inaccurate quantatively. This approach also causes numerical instabilities and locking in coarse discretizations or otherwise pose a prohibitive restriction on the size of the time step. We propose a novel approach to alleviate these issues by replacing indirect volume preservation using Poisson's ratios with direct enforcement of zonal volume constraints, while controlling fine-scale volumetric deformation through a cell-wise penalty. To increase realism, we propose an epidermis model to mimic the dramatically higher surface stiffness on real skinned bodies. We demonstrate that our method produces stable realistic deformations with precise volume preservation but without locking artifacts. Due to the volume preservation not being tied to mesh discretization, our method also allows a resolution consistent simulation of incompressible materials.

Lay Summary

Volume preservation is an important feature in simulation of biological tissues. However, current methods in computer graphics either lose significant volume under deformation, or result in "locking" where the material appears unnaturally stiff. In this thesis we propose a solution to resolve this problem by preserving volumes in anatomical zones instead of local elements, and controlling local volume through a novel inversion-avoidant penalty. We also propose a simple model of the epidermis that provides a more "organic" deformation, where sharp edges are smoothed out.

Preface

All the work presented in this thesis is a product of a collaboration between Seung Heon Sheen, Egor Larionov, Ye Fan, Dinesh Pai, and Vital Mechanics Research Inc. Pai proposed the volume preservation constraint and the epidermis model and supervised the research. Sheen developed the ideas further and implemented all the software for the volume preservation and the epidermis models. Vital Mechanics contributed the simulation mesh and the data for Figure 7.9 and the soft tissue simulation code used in this research. Larionov and Fan contributed to discussions and the soft tissue simulation code, including the friction model used in Figure 7.9, and helped with writing the paper in preparation for submission to ACM TOG, upon which this thesis is based.

The research was partly funded by Vital Mechanics Research Inc. and NSERC, through an Idea-To-Innovation (I2I) grant.

Table of Contents

List of Tables

List of Figures

Acknowledgments

I would like to express my sincere gratitude to my supervisor, Dinesh Pai, for all the advice and support through my studies. It is thanks to his continued guidance that the past two years were so valuable and enjoyable to me.

I would also like to thank Egor Larionov, Edwin Chen, and Ye Fan for their collaboration and for all the valuable discussions that we had which were a source of so much insight.

Thanks to everyone in the lab, in particular Prashant Sachdeva, Jan Hansen, and Ziheng Liang for their valuable friendships in the lab that made the work environment so delightful.

Last but not the least, I would like to thank my family: my parents Dongwoo Sheen and Youngnan Park, my siblings Yoon and Nara Sheen, and my four dogs, for their love and support.

Chapter 1

Introduction

Elastic materials are ubiquitous in everyday life. Many objects we interact with are organic in nature such as plants, animals, food, and most importantly our own bodies. Interestingly, most organic solids are nearly incompressible (due to their high water content), which makes them particularly difficult to simulate. Human soft tissue, for instance, is essentially incompressible, with a Poisson's ratio close to 0.5 [11]. As a result, much of contemporary research in computer graphics focuses on robust simulation of incompressible hyperelastic solids (see Sec. 3). We focus on the popular Neo-Hookean models, which are relatively simple while including non-linearity and the temptation to control incompressibility by setting Poisson's ratio $\nu \simeq 0.5$.

However, it is impossible to emulate true incompressibility and extremely difficult to simulate even near-incompressibility with this approach. This is because as the material approaches incompressibility $\nu \to 0.5$, the first Lamé parameter $\lambda \to +\infty$ (see Sec. 2 for background). The numerical and visual artifacts arising from the failure to correctly enforce incompressibility is known as *locking*.

There are multiple aspects of locking which are problematic for simulating volume preserving elastic solids. First, high Poisson's ratios make the system stiff, which results in stiffness related issues such as stability, and artificial damping. Somewhat related to this, when using linear tetrahedral elements and element-wise volume constraints, the resulting system becomes highly overconstrained. Another aspect arises from the choice of the constitutive equation, where volumetric stress

depends on λ. In classical FEM theory, Céa's Lemma dictates that the quasi-best approximation error depends not only on mesh discretization error, but also on λ. Hence, when $\lambda \to +\infty$, the finite element solution cannot be a reliable predictor of the solution of the PDE. A more detailed explanation can be found in [8].

There are multiple approaches to tackle this issue: the simplest being just using higher-order elements or hexahedral elements. However, the increased computational cost and difficulty of implementation might not be desirable. Another class of popular methods is non-conforming finite elements (such as the Discontinous Galerkin class of methods), where the additional or non-conforming degrees of freedom allow significant deformation and therefore reduce the stiffness of the system. The last approach includes methods that seek to remove these element-wise constraints through Mixed Finite Elements or coarsened constraints, both of which are related to our method.

Our core idea is to tease apart the concept of *incompressibility*, a constraint on a derivative (the deformation gradient) from the related concept of *volume preservation*, a constraint on an integral (the volume of a finite region of material that we call a "zone"). Incompressibility is enforced per element in the standard Neo-Hookean models, usually implicitly, using an energy term. By contrast, we enforce volume preservation as an explicit constraint on the volume of a zone. Volume preservation gives us considerable flexibility to choose larger zones that span multiple elements, zones that are independent of discretization, and zones that are aligned with meaningful anatomical tissue compartments (muscles, abdomen, breast, etc.). Zones may also overlap (e.g., we can preserve both the total volume of a body, and volumes of important tissue compartments).

A second key idea is that since volume preservation is already enforced using constraints, we can use much smaller values of λ or ν, thereby avoiding locking and related numerical instabilities. This can, of course, lead to volume loss per element but that will be compensated by volume gain in other elements in a zone to preserve volume. In other words, our simulation mesh may be viewed as a type of Arbitrary Lagrangian-Eulerian (ALE) mesh, in which volume is never lost but allowed to flow from one cell to another. Locking is always aggravated when using coarse simulation mesh, but our method allows a stable simulation of volume preserving materials with a coarse mesh. To our knowledge, this technique has not

yet been closely studied with FEM simulations in computer graphics.

Note that λ now controls only element volume, rather than the incompressibility of the material. In the rest of the thesis we will repurpose the first Lamé parameter λ to control volume change *per element*, instead of *zonal* volume change. We will continue to use the term Poisson's ratio (ν) in the classical sense.

Large deformations, especially with moving Dirichlet boundary conditions and contact, may produce severely degenerate (even inverted) elements, and break traditional energy models. This issue has attracted much attention in the community [16, 34, 35]. While our λ values are no longer constrained by volume preservation, there is still a need to penalize extreme volume loss per element to avoid such degeneracies. We address this in Sec. 5 with an amendment to the volume penalty term found in compressible elastic energy models. Additionally, the proposed correction improves the compression response in invertible energies.

Human bodies are covered by a layer of skin, a complex multi-layered structure. The outer layer comprising the epidermis is much stiffer than the underlying tissues, and significantly affects the quality of deformation. We propose a simple model of the epidermis and show that this extension contributes heavily to the appearance of realistic tissue deformation.

A simple illustration of these ideas is given in Figure 1.1. It illustrates the more general scenario in which locking artifacts increase at lower mesh resolutions, whereas our volume preservation is independent of the discretization of the zones.

Figure 7.9 shows the practical relevance of good volume preservation. Close-ups of the belly (yellow boxes) and side waist in front view (red boxes) depict tissue displacement in false color, and yield more insights. We see that the traditional Unconstrained Neo-Hookean (UNH) model compresses under the waistband by losing volume, without significantly extruding tissue away (e,h), whereas our method extrudes tissue more realistically, producing a sharp bulge (g,j) due to volume preservation. Increasing ν doesn't help the UNH models since locking reduces the deformation (f,i).

Contributions: we propose a new approach for simulating human tissues and other soft objects that preserve volume, while avoiding the common pitfalls of standard incompressible elasticity models. In addition to avoiding locking artifacts, our zonal volume constraint formulation makes deformation independent of

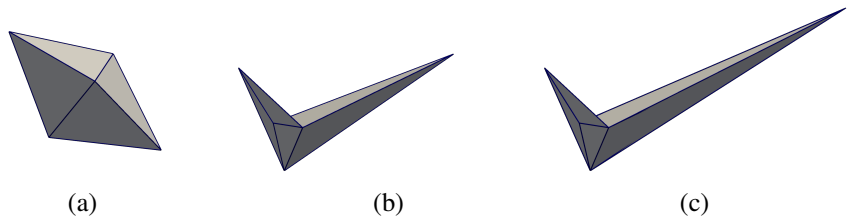

Figure 1.1: Two Tet Simulation: (a) The reference state of the mesh, where two tetrahedrons of equal volume are joined together by a face. The left tetrahedron is constrained by Dirichlet boundary conditions to be compressed into a plane. (b) With an unconstrained Neo-Hookean (UNH) model without the volume constraint, the total volume of the final mesh is 46.628% of the original. (c) With a volume constraint (CNH model), the tetrahedron on the right inflates to twice the volume to keep the total volume constant.

discretization, and allows zones to be aligned with meaningful anatomical tissue compartments. In addition, we repurpose the first Lamé parameter to support inversion robustness and introduce a new form of the compression penalty. We also extend the elastic energy potential to model the stiff epidermis, and demonstrate its importance. Finally, we propose a simple but complete pipeline for assigning volumetric zones using weights on the surface of the volumetric mesh, and demonstrate the application of these methods to predicting the fit of tight fitting garments.

Chapter 2

Background

2.1 Variational Elasticity

In this section, we establish the context for our contributions by introducing FEM simulation of hyperelastic materials as a variational problem.

Let $\Omega \subset \mathbb{R}^3$ be a union of mesh tetrahedra representing an elastic solid in its undeformed configuration. Then let $\mathbf{x} \in \mathbb{R}^{3n}$ correspond to a stacked vector of mesh vertex positions that prescribe the deformation of the solid, where n is the total number of vertices in the mesh. In an elasticity problem, we are interested in finding the configuration $\mathbf{x}$ that results in the lowest potential energy for the elastic solid Ω given a set of boundary conditions and external forces. Mathematically, we may write the problem statement as

$$\mathbf{x}^* := \arg\min_{\mathbf{x}} W(\mathbf{x}), \tag{2.1}$$

where $W(\mathbf{x})$ represents the elastic work function for configuration $\mathbf{x}$. This formulation allows conservative external forces to be added as additional potentials in the objective, however for the sake of simplicity we ignore external forces in the following sections.

With linear (constant strain) elements, W, which is the integral of energy density function $\Psi(\mathbf{x})$, can be written as the sum of volume scaled per-element ener-

gies:

$$W(\mathbf{x}) = \int_{\Omega} \Psi(\mathbf{x}) := \sum_{e} V_e \Psi(\mathbf{F}_e(\mathbf{x})), \tag{2.2}$$

where V_e is the volume of element e in the reference configuration, which depends on the element deformation gradient $\mathbf{F}_e$. The choice of the energy density function Ψ determines the hyperelastic energy model.

For the time discretization, we adopt the implicit Euler time integrator and add an inertial energy term to this minimization, however in this thesis we focus primarily on static FEM for simplicity.

2.2 Incompressibility and Locking

There are two ways in which incompressibility could be enforced: either directly, as a constraint that the volume is preserved, or indirectly with a penalty term that powerfully resists compression. Since both ways are frequently referred to as "incompressible," to avoid confusion we will refer to incompressible Neo-Hookean models using the first method as *"Constrained Neo-Hookean"* (CNH), and those using the second method as *"Unconstrained Neo-Hookean"* (UNH).

Most incompressible hyperelastic energy models used in graphics are of the Unconstrained Neo-Hookean type, and penalize element-wise volume change with a term scaled by the first Lamé parameter λ, which depends on the Young's Modulus E and Poisson's Ratio ν. For instance, the most common version of such an energy density function [7] is written as

$$\Psi_{\text{UNH}}(\mathbf{F};\lambda,\mu) = \frac{\mu}{2}(I_C - 3) - \mu \log J + \frac{\lambda}{2}(\log J)^2 \tag{2.3}$$

where $I_C = \text{tr}(\mathbf{F}^\top \mathbf{F})$ and $J = \det(\mathbf{F})$, which represents the fraction of volume after deformation. This means that when J is close to zero (extreme compression), Ψ_{UNH} will generate large penalty forces to restore the element to reference configuration. Another commonly used material model, co-rotated elasticity [23] is written as

$$\Psi_{\text{CR}}(\mathbf{F};\lambda,\mu) = \mu \|\mathbf{F} - \mathbf{R}\|_F^2 + \frac{\lambda}{2}\,\text{tr}(\mathbf{S} - \mathbf{I})^2,$$

where $\mathbf{R}$ and $\mathbf{S}$ form the polar decomposition: $\mathbf{F} = \mathbf{RS}$ and $\mathbf{I}$ is the 3×3 identity matrix. Here, in a similar fashion, local compression is once again penalized by λ. However, as discussed in the introduction, high Poisson's ratios make the system stiff, which results in stiffness related issues such as instability, and artificial damping.

2.3 Mixed Finite Element Methods

It is often necessary to compute reliable solutions not only for displacements but also for pressures (e.g., for frictional contact or fractures). For displacement-based one-field FEM, pressure must be computed from the displacement variables $\mathbf{x}$. Specifically, cell-wise hydrostatic pressure is usually computed as the negative of the divergence of the Cauchy stress tensor. Since the Cauchy stress tensor is related to the derivative of the energy density function $\Psi(\mathbf{x})$, essentially the pressures computed from a one-field FEM mainly depend on the volume term of Ψ. However, due to similar issues as discussed above, when the material is incompressible and $\lambda \to +\infty$ the volume term stops being a reliable model for volumetric stress.

One traditional way of decoupling incompressibility from λ is by introducing an additional pressure variable $\mathbf{p}$ that models the volumetric stress component of elements, interpolated separately from displacement on the finite element mesh [4]. This allows us to reformulate the variational problem as

$$\mathbf{x}^* := \arg\max_{\mathbf{p}} \min_{\mathbf{x}} \int_{\Omega} \hat{\Psi}(\mathbf{x}) + \mathbf{p}^T \mathbf{c}(\mathbf{x}), \tag{2.4}$$

where $\hat{\Psi}(\mathbf{x})$ is the deviatoric component of the displacement-based elastic potential, and $\mathbf{c}(\mathbf{x})$ is a term that relates $\mathbf{p}$ to $\mathbf{x}$. This additional term can be interpreted as a constraint on $\mathbf{p}$ to be proportional to the hydrostatic pressure computed from the displacements $\mathbf{x}$. Then, $\mathbf{p}$ becomes the Lagrange multiplier for the constraint $\mathbf{c}(\mathbf{x})$. One implementation of this type of formulation is shown in [36]. These methods are known as the displacement-pressure Mixed Finite Element Methods and are one of the most accurate ways to solve the problem.

With the additional degree of freedom, the Babŭska-Brezzi inf-sup condition restricts the choice of the space of finite element basis for the additional variable

for the method to be stable [5]. This condition dictates that the order of basis for the displacement variables must be higher than that of the pressure variables. Specifically, for conforming tetrahedral elements the lowest order finite element space choices are either the Hood-Taylor elements (P_2 for $\mathbf{x}$ / P_1 for $\mathbf{p}$, where P_k denotes the space of k-th order polynomials), or MINI (P_1^+/P_1, where superscript $+$ denotes an enrichment of cubic bubble [2]). Hence, Mixed FEM with a simple linear tetrahedral Finite Element basis for displacement is usually not valid for stable simulations. This includes the Average Nodal Pressure elements proposed in [16], where the Lagrange multipliers of 1-ring volume constraints can be interpreted as cell-wise constant pressure variables (P_0) being averaged on the nodes. Although this alleviates some of the problems arising from each element being constrained, it still fails to meet the inf-sup condition and spurious modes may occur without additional stabilization [29].

Recent research has been focused on developing a stabilized low-order tetrahedral element for incompressible elasticity [32]. Many of these methods allow almost a P_1/P_1 mixed element to be stable and accurate, by adding an additional stabilization term to the FEM basis. However, these methods are still much more expensive than standard linear tetrahedral elements, since the additional pressure variables cannot be solved with simple constraints and require a specific mixed FEM system to be built and solved. The intuition for our approach from these works is that, to achieve an efficient and stable computation of the additional pressure variables, one must sample the pressure variables in a coarser scale compared to the displacement variables. Then, we are able to split the pressure computation into a coarser and finer scale, to control the coarse-scale pressures as separate pressure variables as Lagrange multipliers for volume constraints, as in Eq.2.4, and compute the fine-scale pressures from displacements. Therefore, we look to a much more efficient and simpler approach by enforcing a volume constraint for a few larger zones of elements, and modeling the element-wise local pressure as an additional penalty term.

Chapter 3

Related Work

A number of recent contributions have significantly improved the performance and behavior of hyperelastic solid simulations. The standard approach is using the Finite Element Method (FEM) on a Lagrangian tetrahedral (or hexahedral) mesh [33]. The methods used for soft tissue simulations are typically split between linear and non-linear hyperelasticity models. A number of popular elasticity models are used for soft tissue simulation including Neo-Hookean, St. Venant-Kirchhoff, and co-rotated elasticity.

Co-rotated elasticity [23, 25], has been tremendously successful in real-time and interactive applications largely due to its simplicity. However, it suffers from element degeneration in large deformations [9] and has poor volume preservation properties [34]. Non-linear energy models like the Neo-Hookean models [7], have been used to circumvent these issues at a larger computational cost; although in recent years, Neo-Hookean elasticity has also appeared in interactive simulations [21].

Our work targets invariant based non-linear hyperelastic models, such as Neo-Hookean elasticity, for their generality, superb handling of large deformations and inherent reflection stability.

Among non-linear elastic models are compressible and incompressible hyperelastic models. While incompressible models [24, 30] pose an explicit volume constraint on each element, compressible models prevent severe compression using a penalty term [7]. The most popular method for solving elasticity problems in

computer graphics is the standard linear FEM on a Lagrangian mesh because of its performance profile and versatility. Unfortunately, imposing a severe penalty — let alone a hard constraint — for volume change on each element can cause severe numerical instabilities and locking especially in linear tetrahedral FEM.

In traditional FEM, volumetric locking is addressed by decoupling incompressibility from displacements with Mixed Finite Element Methods. In computer graphics, Irving et al. [16] have addressed locking in tetrahedral meshes by softly constraining the volume of the one ring around each vertex in a tetrahedral mesh using position and velocity correction steps. This approach is an application of nodal strain elements [6], where stress and stain, in this case their volumetric component, is nodally interpolated in a mixed FEM. However, without additional stabilization of some sort, these types of mixed elements are known to be unstable and the number of additional pressure variables are proportional to the number of nodes. A further discussion of Mixed Finite Element Methods was presented in Chapter 2. Kaufmann et al. [19] looked to solve locking by introducing additional degrees of freedom to the system by using a Discontinuous Galerkin discretization. Smith et al. [34] proposed the Stable Neo-Hookean energy model to handle invertible elements as well as improve stability for high Poisson's ratios.

Irving et al. [16] was an implementation of the Average Nodal Pressure element [6], where the cell-wise constant pressure samples of the one-ring neighbors are averaged on the nodes. By contrast, our method uses pressure samples (i.e. the volume preserving zones) that are coarser and decoupled from the mesh topology. Fine-scale cell-wise pressures are instead controlled through a local penalty, which avoids additional pressure variables. This way we can keep λ low enough to avoid locking, while simultaneously enforce volume preservation. Our method has significantly fewer constraints, compared to the total number of vertices, which permits enforcing constraints exactly using constraint minimization to solve the variational problem rather than using constraint projection.

Some works have targeted global volume preservation [10, 13, 14, 28], however not in the context of volumetric FEM. Global volume constraints have also been applied in studies in skinning methods [31]. Some also proposed using a sweep-based approach to conserve the volume [1, 44] or a vector field approach [38]. In contrast, we propose zonal volume constraints for Neo-Hookean type energy

models for Lagrangian FEM simulations.

Finite element simulations also suffer from element inversions during severe deformation. Inversion stability allows simulations to handle large deformations and permits taking large time steps, which can improve simulation performance significantly. A line of recent work has proposed methods for resolving element inversions by extending the energy density function to the negative volume region. Force filtering methods [15, 37] have improved inversion stability but suffer from subtle problems including invalid inversion recovery directions or derivative drift as thoroughly explored in [34]. Stomakhin et al. [35] propose a C^1 or C^2 extension of the entire energy density function for low volume fractions, which resolves many of these problems. However, filtering methods can be quite sensitive to appropriate specification of filtering thresholds and reflection conventions [41]. We instead follow a simpler approach similar to [34], where we design a volumetric penalty term to satisfy necessary conditions for stability and inversion robustness. Our penalty function improves upon the Stable Neo-Hookean volumetric term by introducing nonlinearity to the stress also, resulting in better inversion recovery and improved performance.

Chapter 4

Zonal Volume Constraint

To solve the problem of volumetric locking, instead of enforcing a per-tetrahedron near-incompressibility with high Poisson's ratio, we adopt the approach of Mixed Finite Element Method as in 2.4. Essentially, we solve the saddle-point system as a constrained minimization with constraint function $\mathbf{c}(\mathbf{x}) = \mathbf{0}$. Specifically, our constraint enforces the total volumes of zones defined as local sets of finite elements to be preserved. Compared to other mixed elements, our approach is much more efficient and easier to implement while showing comparable results. Moreover, our approach provides the modeling flexibility of choosing zones that are aligned with anatomical compartments (see Section 6).

Each constraint is simply formulated as the requirement that the total volume of all elements in a specified zone of the deformed mesh is equal to the initial volume. That is, for j-th zone G_j, the zonal volume constraint function c_j is defined as follows,

$$c_j(\mathbf{x}) = \sum_{e \in \zeta_j} V_e(\mathbf{x}) - V_e^0, \tag{4.1}$$

where V_e^0 is the reference volume of element e, which belongs to zone j with element index set ζ_j.

Imposing this constraint for each zone gives us a new constrained minimization

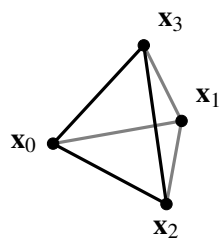

Figure 4.1: A sample tetrahedral element, with 4 vertices at positions $\mathbf{x}_0$, $\mathbf{x}_1$, $\mathbf{x}_2$, and $\mathbf{x}_3$.

problem:

$$\min_{\mathbf{x}} \int_{\Omega} \Psi(\mathbf{x}) \tag{4.2}$$

$$\text{s.t. } c_j(\mathbf{x}) = 0 \quad \forall j. \tag{4.3}$$

As a special case we can preserve the total volume with a single *global* constraint; by contrast, classical incompressible Neo-Hookean models require the volume of each and every element to be preserved.

To illustrate the simplicity of this type of constraint we define the volume constraint for a tetrahedral mesh. The volume of the tetrahedron e, as depicted in Figure 4.1, is defined (up to a constant scaling) as the triple scalar product

$$V_e(\mathbf{x}) = \mathbf{v}_3 \cdot (\mathbf{v}_1 \times \mathbf{v}_2),$$

where $\mathbf{v}_i = \mathbf{x}_i - \mathbf{x}_0$. Then the Jacobian of the constraint function can be computed as

$$\frac{\partial c_j}{\partial \mathbf{x}} = \sum_e \frac{\partial V_e}{\partial \mathbf{x}},$$

where the sparse vector $\frac{\partial V_e}{\partial \mathbf{x}} \in \mathbb{R}^{3n}$ is zero everywhere except for the vertices of element e, where

$$\left[\frac{\partial V_e}{\partial \mathbf{x}}\right]_0 = -(\mathbf{v}_2 \times \mathbf{v}_3 + \mathbf{v}_3 \times \mathbf{v}_1 + \mathbf{v}_1 \times \mathbf{v}_2)$$

$$\left[\frac{\partial V_e}{\partial \mathbf{x}}\right]_1 = \mathbf{v}_2 \times \mathbf{v}_3, \quad \left[\frac{\partial V_e}{\partial \mathbf{x}}\right]_2 = \mathbf{v}_3 \times \mathbf{v}_1, \quad \left[\frac{\partial V_e}{\partial \mathbf{x}}\right]_3 = \mathbf{v}_1 \times \mathbf{v}_2.$$

Finally, the Hessian stencils for each V_e will be simple linear skew-symmetric matrices. Thus, $c_j(\mathbf{x}) = 0$ is a one dimensional constraint with simple to implement sparse derivatives, which gives true volume preservation. Note that this constraint can be further optimized by computing the volume of the entire zone by iterating over zone boundary faces only.

Although uncomplicated, this constraint provides a powerful tool for emulating incompressible elasticity. It allows users to achieve volume preservation without increasing Poisson's ratio, which can cause instabilities and locking. For most nonlinear solvers a few equality constraints should not be prohibitively expensive to solve, but for additional performance gain one may naturally use an Augmented Lagrangian method to solve the constraints.

The zone sizes are important in determining the level of local incompressibility. One global zone for the entire mesh will essentially be a hydrostatic simulation, analogous to simulating a water balloon. As the zone sizes decrease, there will be more local incompressibility around each element which will result in a stiffer behavior. However, as long as the zones are at least as large as the 1-ring [16], volumetric locking will not occur. Therefore, as we use a smaller zone sizing, the results will become more similar to the results in [16], but at a steeper performance cost.

Our method can be viewed as a simplification of the 2-field mixed formulation (2.4), where the pressure potential is given as

$$\mathbf{p}^T \mathbf{c}(\mathbf{x}) = \sum_j \mathbf{p}_j c_j(\mathbf{x}) = \sum_j \mathbf{p}_j \left(\sum_{e \in G_j} V_e(\mathbf{x}) - V_e^0 \right), \tag{4.4}$$

where the interpolated hydrostatic pressures $\mathbf{p}_j$ for zone j are identified to be the Lagrange multipliers for the j-th zonal volume constraint. If each element was assigned to a unique zone, our method would recreate the mixed-element formulation for incompressible materials. However, we use only a handful of zones, which keeps the problem size small and avoids locking and instability.

An important advantage of enforcing volume preservation with zonal con-

straints is that it allows a way of simulating incompressible objects using a much coarser mesh than by using a traditional 1-field method. Céa's lemma already couples the quasi-best approximation error with mesh resolution, and since a 1-field FE solutions also couple the bulk modulus to the upper bound of the approximation error, it makes it even harder to use a coarser mesh when bulk modulus is high. However, when incompressibility is decoupled from the bulk modulus, and we can use much smaller λ, we are able to achieve simulation results of a fine-mesh simulation that is consistent with a much coarser mesh. Figure 7.6 shows a simple dynamic simulation with a very fine mesh, and Figure 7.7 shows the same simulation using a much coarser mesh. We see that both the low Poisson ratio and our method achieves consistent visual results between the fine and coarse case, but the high Poisson ratio case fails to converge very early in the simulation.

4.1 Stabilization

We apply the F-bar method [26] to the energy density function to ensure stability. This is based on a multiplicative split of the deformation gradient $\mathbf{F}$ into a deviatoric and volumetric component. The deviatoric part is computed as

$$\bar{\mathbf{F}} = \alpha \mathbf{F}, \tag{4.5}$$

where

$$\alpha = \frac{\bar{J}^{\frac{1}{3}}}{J^{\frac{1}{3}}}, \tag{4.6}$$

and $\bar{J}$ is the average of J computed over a set of local element stencils. In our case, the local setss are the zones where the total volume is preserved, hence conveniently $\bar{J} = 1$, and $\alpha = J^{-\frac{1}{3}}$. However, since as $J \to 0$ we have that $\alpha \to +\inf$, we instead apply a C-2 extension to α below a certain threshold ε, similarly to [35]. Then the new extended deviatoric projector is given as

$$\tilde{\alpha} := \begin{cases} J^{-\frac{1}{3}} & \text{for } J > \varepsilon \\ \varepsilon^{-\frac{1}{3}} - \frac{1}{3}\varepsilon^{-\frac{4}{3}}(J-\varepsilon) + \frac{2}{9}\varepsilon^{-\frac{7}{3}}(J-\varepsilon)^2 & \text{for } J \leq \varepsilon \end{cases} \tag{4.7}$$

In practice, the choice of ε is not too important as long as it is small (~ 0.1).

We then use $\bar{\mathbf{F}}(\mathbf{x})$ to compute the deviatoric part of the constitutive equation. For example, the deviatoric part of Neo-Hookean energy density function (2.3) will now be computed as

$$\bar{\Psi}_{\mathrm{NH}}(\bar{\mathbf{F}};\lambda,\mu) = \frac{\mu}{2}(\tilde{\alpha}^2 I_C - 3). \tag{4.8}$$

Note that this is similar to the form presented by [30], but extended below ε to be continuously defined for $J \leq \varepsilon$.

Using only the deviatoric component of deformation gradient for the elastic potential energy, we remove the contribution of the constitutive equation on the pressure. Hence, this allows the complete split of the total elastic stress, to the deviatoric stress from the elastic potential, and the volumetric stress from the constraint Lagrange multipliers and the volume penalty.

Chapter 5

Volume Penalty

Our method ensures that volume is preserved within each zone, but without any element-wise volume change penalty the volume inside each zone can transfer between elements. This is a feature, as discussed in the Introduction, since it reduces the cost and numerical challenges of enforcing volume preservation locally, while ensuring good behavior globally. Note that, unlike in the hydrostatic case, volume can not transfer completely freely since elastic forces due to the shear modulus restrict large flows.

However, the zonal constraints by themselves model only the hydrostatic pressure in the coarse zones, hence we also need to model the finer-scale pressures in the individual elements. We employ a more traditional approach to modeling element-wise pressure in the penalty method. To model this local compression penalty function, we look at the volume penalty functions present in various Neo-Hookean elasticity models. In Neo-Hookean models, the bulk modulus models how much the material resists element-wise volumetric deformation. The bulk moudulus is represented in most Neo-Hookean energy formulations in the first Lamé parameter λ, which is a combination of the shear and bulk modulus. However, as discussed in Section 2, when $\lambda \to +\infty$ locking occurs, and the pressure computations become unstable. But since we model the coarse-scale pressures as constraints, and we only need to model the finer-scale deviations in pressures, we are able to use a lower λ and avoid locking.

If λ is set too low the simulation is more susceptible to collapsing elements

and even equilibrium configurations with inverted elements for invertible energy models. Consider the example in Figure 7.5 of a cylindrical puck with a moving Dirichlet boundary condition on a set of vertices on top of the puck. As the puck compresses, the tetrahedra underneath the moving boundary are flattened to the point where subsequent steps cause boundary adjacent tetrahedra to invert. At this point, incompressible energy models with a logarithmic volume penalty ($\log J$) term will become undefined because $J \leq 0$. Other models, like co-rotated elasticity, may permit inverted elements, but won't be able to recover from an inverted configuration. This issue has motivated a number of solutions [15, 34] for handling inverted elements, but we will focus on the recent work on the Stable Neo-Hookean model developed by Smith et al. While the proposed model attempts to solve many of the issues with non-invertible energies and doesn't require additional parameters, as can be seen from the plot of the volume change penalty term in terms of relative volume change J in Figure 5.1, the Stable Neo-Hookean energy resists compression much more timidly as compared to the standard Neo-Hookean model defined in Equation (2.3).

This results in the simulation possibly converging to an invalid configuration where inverted elements exist, and a nonlinear optimization solver can struggle due to inverted elements being present in intermediate solutions which cause oscillations. Especially, this oscillation can be aggravated when constraints are introduced, presenting major performance issues when one tries to use volume constraints.

This suggests a need for a good penalty term that is both invertible and still resists compression effectively. Let us write such penalty term as $U(J)$, controlled linearly by parameter λ. To design such a penalty term, we first take a look at what conditions the function $U(J)$ must meet.

A detailed study of various Neo-Hookean compression penalty terms and explanations for each of the conditions can be found in [12].

a) The function must evaluate to 0 at rest ($J = 1$).

b) The gradient of the function, i.e the volumetric stress, must also evaluate to 0 at rest.

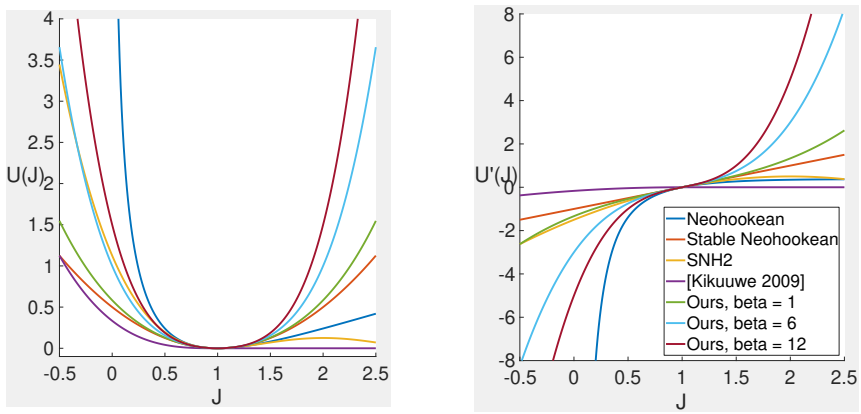

(a) (b)

Figure 5.1: Penalty Plots: A plot of the penalty terms $U(J)$ and their stresses $U'(J)$ from different energy formulations (Neo-Hookean, Stable Neo-Hookean [34], the second-order expanded version of Stable Neo-hookean, [20], ours with $\beta = 1$, and ours with $\beta = 6$) with $\lambda = 1$, in terms of the relative volume change J. The Neo-Hookean volume term (blue) indicates a substantially larger penalty when compared to Stable Neo-Hookean (orange) and [20] (yellow), but the penalty term is undefined when $J \leq 0$ due to its log term. This is more evident to see in the stress plot during compression ($J < 1$), where the Stable Neo-Hookean volumetric stress changes in a linear manner. Our method for both $\beta = 1$ (purple) and $\beta = 6$ (green) shows much more effective penalization under compression and stretch. Our stresses shows a nonlinear dependence on J similar to the Neo-Hookean term, but also shows a effective growth not only during compression but also during stretch.

c) For the λ of the penalty term to correspond to the Lamé parameter in linear elasticity, $\frac{\partial^2 U(1)}{\partial J^2} = 1$ must hold.

d) The function must be defined for all real numbers $(-\infty, +\infty)$.

e) $\frac{\partial^2 U(J)}{\partial J^2} \geq 0, \forall J \in \mathbb{R}$ for the penalty to both penalize compression and stretch.

Consider the following function,

$$U(J;\beta) := \frac{1}{12}(J-1)^2\left[\beta(J-1)^2 + 6\right], \tag{5.1}$$

where the parameter $\beta \in [0, +\infty)$ controls how steeply the penalty function will penalize change in J. The first and second derivatives of the function are

$$\frac{\partial U(J;\beta)}{\partial J} = \frac{1}{3}(J-1)\left[\beta(J-1)^2+3\right], \text{ and} \tag{5.2}$$

$$\frac{\partial^2 U(J;\beta)}{\partial J^2} = \beta(J-1)^2+1. \tag{5.3}$$

Therefore, the function satisfies all of the conditions listed above. Note that for $\beta = 0$, $U(J;0) = U_{\text{SNH}}(J) = \frac{1}{2}(J-1)^2$. As β is increases, the penalty function penalizes compression and stretch more effectively than the Stable Neo-Hookean penalty term, while still being fully invertible. Therefore, this is a suitable choice for our compression penalty term. Plots comparing different penalty terms $U(J)$ and stresses $\frac{\partial U(J)}{\partial J}$ are shown in Figure 5.1. Experimentally, $\beta = 1$ was sufficient for most realistic examples governed by external force, but for examples where inversions were more likely due to contact or boundary conditions, we could easily find higher β that resolves all inversions.

The additional nonlinearity introduced in the gradient (Equation (5.3)) of our penalty function compared to a standard Stable Neo-Hookean penalty is the main reason for the inversion-robustness in our model. It is possible to formulate models with even higher nonlinearity than what we propose here, but in our experiments we found that such energy models provide no significant benefit in resolving inversions compared to (5.1) and only increase the number of nonlinear solver iterations until convergence. We discuss this further in Appendix A.

We demonstrate that by this simple addition to the energy potential, we can obtain results similar to that of using mixed finite elements as in [16], but with very few or even one global constraint. The results of Figure 7.3 demonstrate that with a penalty of about $\nu = 0.45$ and with just one global zone, the deformations are close to using a 1-ring constraint around each vertex.

Also, we found that simply adding this additional nonlinearity to the energy resulted in faster performances in most examples when volume constraint was used, and even in many cases where there were no constraints. In Table 7.1, we compare the performance results of using $\beta = 0$ (equivalent to SNH) and higher β.

Chapter 6

Volumetric Zoning

For a more complete description of the pipeline, we propose a simple method of obtaining volumetric zones on a tetrahedral mesh from surface vertex annotation.

Manual vertex painting is a very common part of many character animation pipelines, allowing users to assign attributes such as skinning weights. Alternatively, there are methods to automatically compute transformation weights from skeleton meshes [3, 31, 42], from sparse subsets of degrees of freedom [17], or from animation data [18].

Using either of the aforementioned methods, we end up with a set of weights defining possibly overlapping zones on the surface of our FEM mesh. We then transfer this data onto the surface triangles. Naturally these surface zones should be simply connected in order for the volumetric zones to follow suit.

In order to transfer zone information to the rest of the tetrahedral mesh, we first construct a smooth potential field around the mesh surface using Hermite Radial Basis Functions [22, 27, 39, 43], although any signed distance field will do. We then project each tetrahedron centroid along the potential gradient onto the surface triangles. The triangle zone information is then copied from the triangles, back to the source tetrahedra.

Albeit simple, this projection is an effective method to map internal tetrahedral mesh elements to surface triangles. This way, we allow the users to define volume preserving zones by simply painting surface vertices with any existing tool. We demonstrate this approach with an sample female body simulation mesh on Fig-

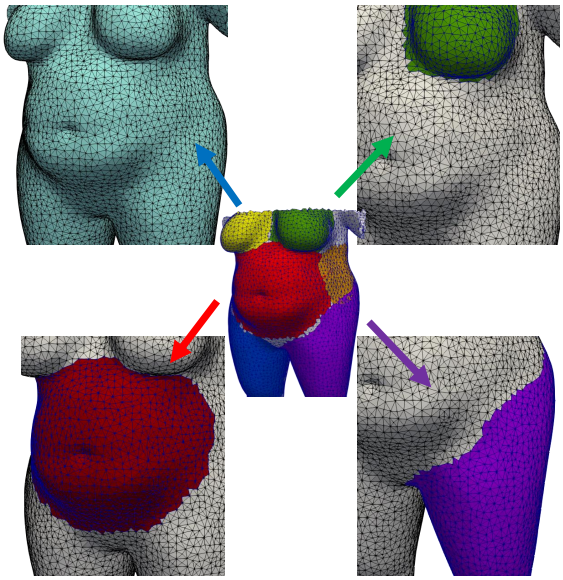

Figure 6.1: Body Zones: Volume preserving zones on the body mesh used for simulation in Figure 7.9. Six significant anatomical compartments (belly (red), side and back waist (orange), 2 legs (blue and purple), 2 breasts (yellow and green)) are selected as zones. Additionally, another zone is added including the full body (cyan), so that the entire body would be volume preserving. Note that the full body zone is not necessary, but can be added to ensure the volume preservation of not only each compartments but also the entire body. The zones are drawn on the mesh surface with a texture painting tool in a visual effects software, and then projected to the inner body using our projection method.

ure 6.1, where the surface zones are chosen manually to capture the anatomical volume-preserving regions.

Chapter 7

Results

The following results demonstrate the versatility of our method. We use a tetrahedral mesh discretization for all our simulations.

Our implementation relied on the Ipopt non-linear optimization package [40] to solve the constrained optimization problem proposed in equation (4.3). In our experiments, we found that excessive parameter tuning was not required to use our method with Ipopt: only when used with additional nonlinear constraints, we occasionally tuned the texttnlp˙scaling˙max˙gradient parameter.

For all our examples except for Twist (Figure 7.1), we started with $\beta = 1.0$ and increased to improve performance. However, for just resolving inversions and numerical instability, $\beta = 1.0$ works well for all of those examples.

7.1 Two Tetrahedrons

As the most simple proof of concept example for the volume constraint, we design a mesh with two tetrahedrons with equal volume joined together by a face as shown in Figure 1.1. We then compress one of the tetrahedrons with a Dirichlet boundary condition to a plane, to see the effects of the volume constraint. The energy model used is Neo-Hookean with $\nu = 0.495$.

As expected, the example without the global volume constraint loses around 50% of the volume, since the deformation of the compressed tetrahedron does not affect its neighbor. When a volume constraint is applied, the unconstrained

tetrahedron inflates to twice the original size, keeping the total volume constant.

7.2 Twist

We adopt the classic twisting cube test to verify the robustness of our method. We fix the two sides of a 15^3 cube, and twist one of the fixed sides by $\frac{\pi}{2}$ three times. With $\mu = 4.0, \lambda = 100.0$ the basic Stable Neo-Hookean simulation loses 6.45% of the volume in the initial two rotations, then collapses from severe inversions. Adding additional non-linearity to the volumetric energy density function of $\beta = 9.0$, we are able to completely remove the inversions and achieve a robust simulation to the end, while the volume error remains almost the same. By imposing a volume constraint on the global zone, the volume is preserved completely. Finally, adding an epidermis model of $\lambda = 15.0, \gamma = 1.0$ results in a more organic surface deformation.

7.3 Stretch

We demonstrate the inversion robustness and performance of our method with a stretching cube example, where a regularly discretized cube of dimensions $20 \times 20 \times 20$ is stretched to 8 times its original length. In all cases, $\mu = 1.0$, and the relative tolerance for Ipopt was $1e-6$. Using an unconstrained Stable Neo-Hookean energy with $\lambda = 10.0$ (or $\nu \approx 0.4545$), the runtime was 2.803 seconds per frame. However, there were severe tet inversions in the final frames and the volume error was 14.83%. With $\lambda = 100.0$ (or $\nu = 0.495$) the tet inversions were removed and the volume error was reduced to 5.05%, but the runtime per frame increased to 9.905 seconds per frame.

With the volume constraint added and using a penalty of $\lambda = 25, \beta = 0$ (equivalent to Stable Neo-Hookean), the runtime per frame was 7.892 seconds. The inversions were completely removed and the volume was accurately preserved. By increasing β to 1, the performance improved by 8.38% to 7.282 seconds per frame. When epidermis ($\lambda_e = 10.0, \gamma = 1.0$) was added, the performance improved to 6.251 seconds per frame, while producing a more organic looking result.

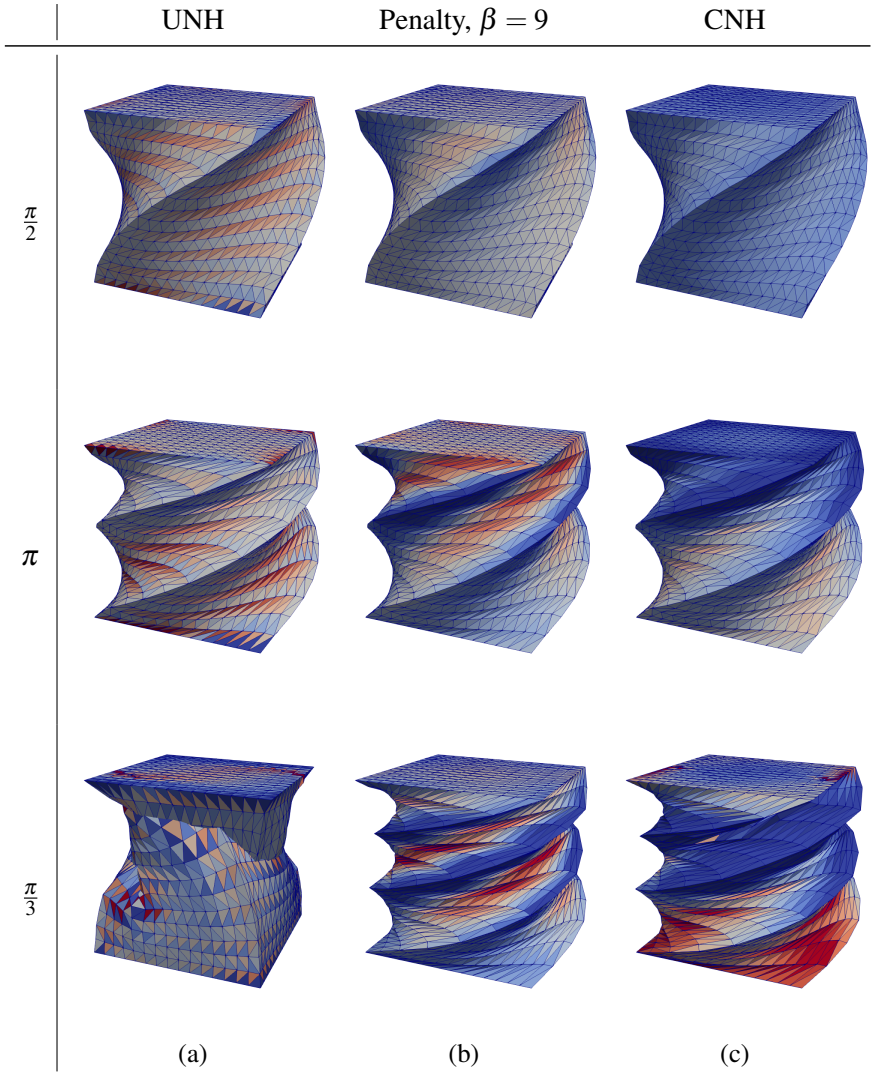

Figure 7.1: Twist: The top face of a cube is rotated by $\frac{\pi}{2}$ (top row), by π (middle row), and by $\frac{3\pi}{2}$. (a) is a UNH simulation using the Stable Neo-Hookean model with $\lambda = 100$, (b) is a UNH simulation using a local compression penalty with $\lambda = 100, \beta = 9$, (c) is a constrained simulation where a global volume constraint is added. Notice that where the Stable Neo-Hookean simulation fails, the additional non-linearity introduced by the compression penalty successfully resolves inversions. Adding the volume constraint allows a completely incompressible simulation.

(a) UNH, $\lambda = 10$

(b) UNH, $\lambda = 100$

(c) CNH, $\lambda = 25$

(d) CNH + Epidermis

Figure 7.2: Stretch: A cube is stretched to eight times of its original length. (a) Using the unconstrained SNH with $\nu \approx 0.4545$, the volume error was 14.83% and tets became inverted around the cube corners (purple tets). (b) With $\nu = 0.495$, inverted tets were removed and the volume error is reduced to 5.05%. (c) When volume constraint ($\lambda = 25, \beta = 1$) is introduced, the volume is completely preserved and the simulation is 26.54% faster. (d) With the epidermis ($\lambda_e = 10, \gamma = 1$) the deformed surface is regularized and the resulting deformation looks more organic.

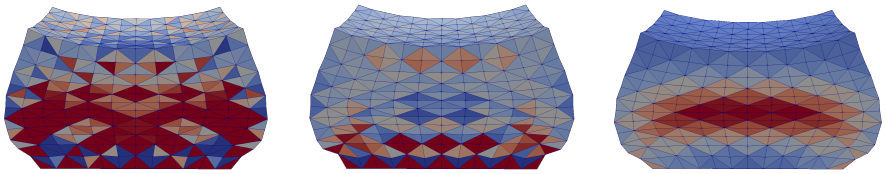

(a) UNH, $\nu = 0.495$ (b) One-ring (c) CNH, $\lambda = 100, \beta = 1$

Figure 7.3: Pressure Distribution: A cube with 12^3 vertices is suspended under gravity with the bottom surface fixed with Dirichlet boundary conditions, visualized with the per-tet pressure distribution in the inner body. (a) shows the per-tet Poisson's ratio approach with $\nu = 0.495$, where the effects of volumetric locking results in highly irregular pressure distribution. (b) is the result where a one-ring volume constraint is used, where a checkerboard pattern appears in the pressure distribution due to a lack of stability. Finally, (c) is our method with $\lambda = 100, \beta = 1$, where the pressure distribution is regular and realistic.

7.4 Pressure Distribution

Following a classic volumetric locking example, we test our methods with a standing cube simulation. A Neo-Hookean cube with shear modulus $\mu = 10.0$ is suspended under gravity with the bottom surface fixed with Dirichlet boundary conditions, results shown in Figure 7.3. This example demonstrates the effects of external force on the pressure distribution on the body surface and interior with regards to different approaches of simulating incompressibility. Irregular pressure distribution may not visually affect the results much, but when simulating frictional contact or fracture, they might result in unrealistic solutions. The high Poisson's ratio ($\nu = 0.495$) approach results in obvious irregularities in the pressure distribution, a manifestation of volumetric locking. The per-tet hydrostatic pressures in this case are computed as the the volumetric components of the stress tensors, that is, the negative divergence of the Cauchy stress. The high bulk modulus per each element causes pressure computation from displacement variables to be unreliable. The one-ring volume constraint approach [16], which is equivalent to the Average Nodal Pressure element [6], shows a more regular pressure distribution, but also shows checkerboard patterns. In this case, the pressures are the Lagrange multipliers for the volume constraints, scaled to be in the same units as the vol-

umetric stress then mapped back to the cells. The checkerboard pattern is an artifact of the instability of the one-ring constraint approach, where the averaging of the pressure variables on the nodes allows solutions with such checkerboarding to occur. With our method with one global zone and a local compression penalty of $\lambda = 100, \beta = 1$, we compute the per-tet pressure as a sum of the average zonal pressure (the Lagrange multiplier of the zonal volume constraint) and the fine-scale pressures computed from the volumetric stress component from the penalty. Then since the bulk modulus is much smaller, as opposed to $(\nu = 0.495) \equiv (\lambda = 400)$ in the Poisson's ratio approach, volumetric locking does not happen from the penalty, and therefore the volumetric stress components are more regular. Since the volume preserving zone is global and since the average pressure is constant throughout the zone, checkerboard pattern in the Lagrange multipliers is not an issue.

7.5 Dynamic Stability

We test the stability of our method in dyanamic simulations compared to [16] and a naïve volume rescaling method. We simulate a cube consisting of 16^3 cells with $\mu = 100.0$ is subjected under gravity. We tested the simulation with a timestep of 8ms for a total of 1000 frames. We found that the volume projection in the Irving algorithm can be unstable when used with large timesteps, and a clamping of volume preservation forces must be applied to make it stable. However, we found that the clamping threshold to make this specific example not blow up was quite low, resulting in a volume error of 2.4% at worst. Even with such aggressive clamping, we noticed visible oscillations on the top surface of the cube. We also tested a simple volume rescaling algorithm, where the mesh was projected every time step based on its center of mass, such that the global volume is conserved. We found that this method is highly unstable and virtually impossible with Semi-Implicit Euler integration (where only one Newton step is used) without increasing Poisson Ratio to higher than 0.495, where then locking occurs instead. With full Backwards Euler integration, we could get the simulation to not blow up, but it still required a quite high Poisson Ratio of 0.48. However, a unrealistically exaggerated oscillation of the entire mesh was present even until the final frames. Compared to the other methods, we found our method to be very stable, and the runtimes were

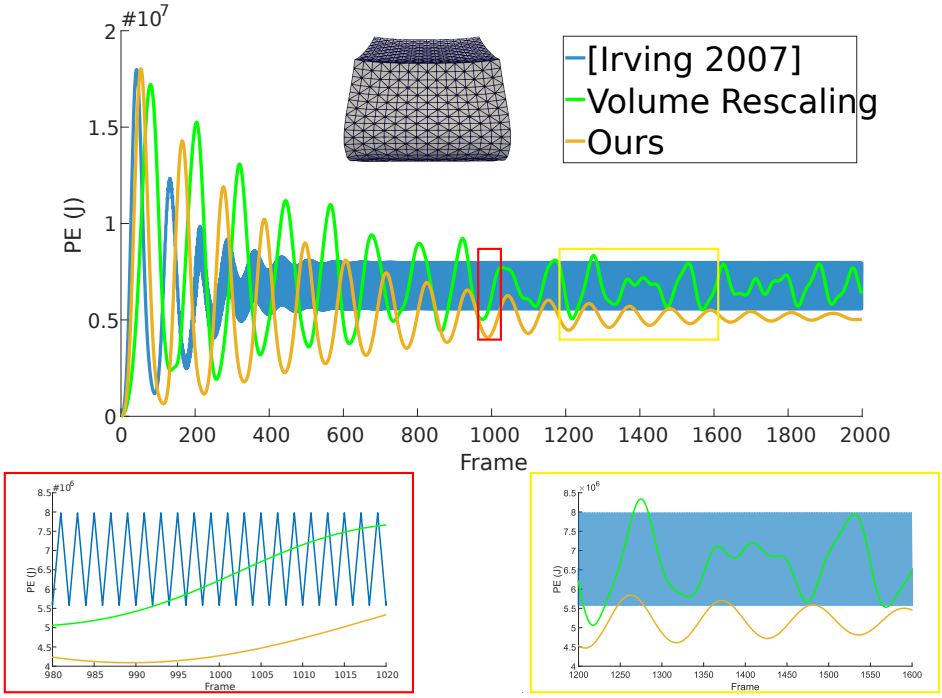

Figure 7.4: Dynamic Stability: Energy plot from the simulation of a soft 16^3 cell cube subjected to gravity, with a moderately large timestep of 8ms. We compare three different algorithms for simulating incompressibility, where the blue curve is the energy plot for the one-ring pressure algorithm of [16], the red is a naïve global volume rescaling algorithm, and yellow is ours. [16] (blue) shows severe instability even with an aggressive clamping of the volume recovery. Note how due to the extreme oscillations in potential energy, the energy plot for the method appears as a thick line in the top plot. The bottom plots show a magnified plot to demonstrate how the energy behaves in small timeframes. The volume rescaling algorithm (green) gains and loses energy arbitrarily due to a unrealistic simulation of the volumetric stress, which can be seen from the irregularities in the plot. Our method (yellow) displays a realistic and stable energy behavior, and converges to a stable configuration.

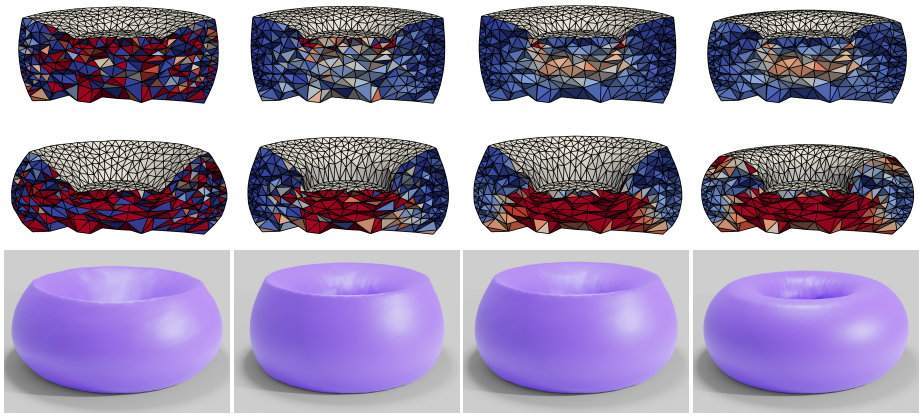

(a) UNH, $\nu = 0.495$ (b) UNH, $\nu = 0.4545$ (c) CNH (d) CNH + Epidermis

Figure 7.5: Bulge Test: A cross-section of a simulated puck is shown. The puck is indented at 25% and 50% of its height. (a) is the result without volume constraint and $\nu = 0.495$. These base results show visible volume loss of 0.6% and 1.8% and artificial stiffness from locking, resulting in no visible bulging at the cylinder top. Also, the pressure distribution visualized by the color scheme shows severe irregularities. (b) is the simulation with $\nu = 0.4545$, which loses 2.1% and 5.1% of the total volume respectively. (c) shows the result with volume constraint and $\lambda = 100$ and $\beta = 9$, showing a realistic bulging due to successful volume preservation. (d) shows the result where an epidermis of $\lambda = 100$ was added, where the surface demonstrates a more organic deformation due to surface volume preservation.

comparable (around 2% faster) to Irving's, which is a semi-implicit method where ours is fully implicit. With our method, this simulation is stable at much higher timesteps, i.e. 33ms.

The plot of the potential energy for this simulation can be seen Figure 7.4. Note the extreme oscillations present in the potential energy plot for the one-ring nodal pressure algorithm [16] and the unrealistic irregularities in the plot for the volume rescaling algorithm.

7.6 Bulge Test

One good natural example of an incompressible material is the human tissue, so to test the effects of our method, we test on the "skin puck" model from [27], where the vertices on the bottom are fixed with Dirichlet boundary conditions. When simulating biological tissue, bulging is a crucial visual characteristic that depicts the incompressibility of the underlying material. Therefore, it is important that this simulation shows visually significant bulging under compression.

We use a 22K tetrahedron simulation mesh for the puck. To produce substantial compression, we animate a set of vertices on the top of the puck with a Dirichlet boundary condition moving these vertices down by a fixed amount per time step. We performed a quasi-static simulation where at each step, the animated surface is indented by 1% of the height. We test the displacement until 50% of the total height of the puck, which produces extreme compression.

Without the volume constraint, a low Poisson's Ratio $\nu \in [0.0, 0.45]$ will result in little noticeable bulging at the top surface due to volume loss, and a higher ν will result in unnaturally stiff visual results and irregular pressure distribution due to volumetric locking. Also, even at $\nu = 0.495$, there was a 1.8% volume loss at an indentation of 50% of the puck height.

Adding the volume constraint allows a completely incompressible simulation with realistic pressure solutions for this example, without being a heavy burden on the performance in most cases. At 50% indentation, the amount of volume loss can be made arbitrarily low[1] with the global volume constraint using any type of energy model and parameters. In contrast, a standard simulation without the constraint produces approximately 22% volume loss with $\nu = 0.4$, 5.1% loss with $\nu = 0.45$, and 1.8% loss with $\nu = 0.495$. However, without any local compression penalty the simulation converges to an infeasible state with many inverted tets around the border of the Dirichet boundaries.

Adding our local penalty term with $\lambda = 100$ allows the simulation to be completely free of inverted tets. Although even with $\beta = 0$ the solution does not converge to an infeasible state, the lack of a sufficient resistance to volumetric deformation causes numerical instability and results in a very slow convergence of the

[1] Up to machine precision.

nonlinear optimizer during the timesteps with more extreme deformations (after the 25% indentation). By using $\beta = 9$ we were able to achieve better numerical stability, resulting in a 14.84% faster runtime on total, and 21.17% faster runtime when only considering the frames after the 25% indentation where the moving Dirichlet boundary starts to invert elements. Finally, with an epidermis model of $\lambda_e = 100, \beta_e = 1$ added, we are able to generate a more regular surface deformation and achieve an visually organic deformation overall.

7.7 Dynamic Impact

We test a simple dynamic result of a soft ball consisting of 64K tets dropped under gravity and dropped to the ground in Figure 7.6. We used a timestep of 1ms and $\mu = 16.0$ KPa. Using a per-tet Poisson's ratio $\nu = 0.495$ results in the sphere behaving much stiffer than what the material parameters would suggest, while still losing up to 12.7% of its volume. When using a per-tet Poisson's ratio of $\nu = 0.45$, the ball retains its appearance of soft elastic deformation, but loses up to 51% of its original volume. Using our method, we are able to simulate the soft elastic deformations while preserving the volume down to solver accuracy, while being 5.7% faster than the high Poisson's ratio case and only 3.7% slower than the $\nu = 0.45$ case.

7.8 Resolution Consistency

An important advantage of enforcing volume preservation with zonal constraints is that it allows a way of simulating incompressible objects using a much coarser mesh than by using a traditional 1-field method. Céa's lemma already couples the quasi-best approximation error with mesh resolution, and since a 1-field FE solutions also couple the bulk modulus to the upper bound of the approximation error, it makes it even harder to use a coarser mesh when bulk modulus is high. However, when incompressibility is decoupled from the bulk modulus, and we can use much smaller λ, we are able to achieve simulation results of a fine-mesh simulation that is consistent with a much coarser mesh.

When a coarser mesh (4.7K tets) is used, the advantage of our method becomes even clearer to see. For the low Poisson's ratio example, the maximum volume loss

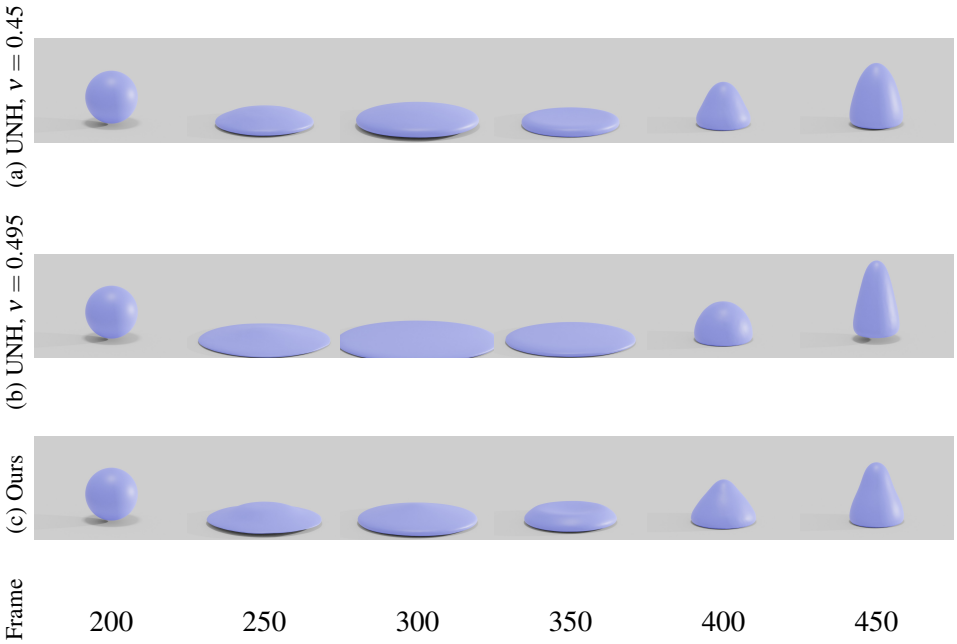

Figure 7.6: Ball Drop: An elastic sphere consisting of 64K tets is dropped to the ground. (a) shows the result with the standard UNH model with per-tet Poisson's ratio $\nu = 0.45$, where the ball loses more than half its volume in the second column. (b) is the UNH result with $\nu = 0.495$, where the volumetric locking makes the ball appear unnaturally stiff. Notice how the ball always retains its spherical shape and just get flattened and stretched in the vertical direction. (c) is the result using our CNH model with global volume constraint and local compression penalty with λ equivalent to $\nu = 0.45$. Note that the volume of the sphere is preserved, producing a nice "squash-and-stretch" effect, and the artificial stiffness is removed.

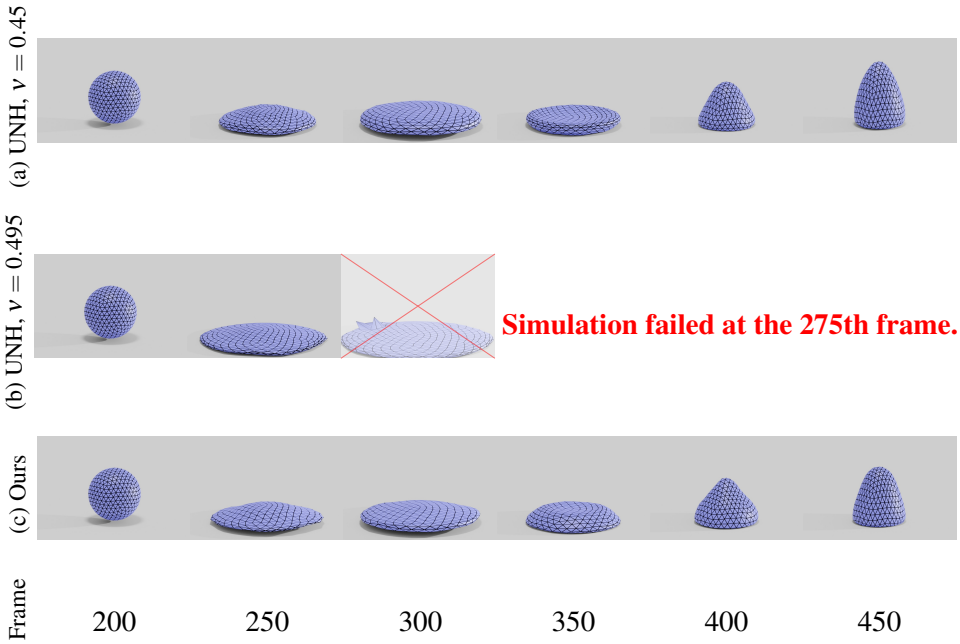

Figure 7.7: Coarse ball: Similarly to Figure 7.6, a much coarser sphere with 4.7K tets is dropped to the ground. (a) shows the UNH result with $\nu = 0.45$, where the ball has lost 52% of its original volume at the 250th Frame, but gain 36% volume at the 300th frame. (b) is the result of using UNH with $\nu = 0.495$, where due to using a coarser mesh the issue of locking is exacerbated, and the simulation fails to converge at the 275th frame. (c) is our result, where the simulation is stable and consistent with the result when using a much finer mesh, demonstrating our advantage of resolution consistency.

is almost equal to when using a finer mesh (52.8%). But after its impact with the ground, the ball actually gains volume due to the severe volumetric deformations resulting in extremely high volumetric elastic force, and the ball gains up to 36.1% of its initial volume. The high Poisson's ratio case fails to converge after the 275th frame (corresponds to the 0.275th second). This failure to converge when using a coarse mesh demonstrates how locking is aggravated when the simulation mesh is coarser, leading to a extremely high approximation error as predicted by Céa's Lemma. However, using our method allows a simulation of a completely volume

preserving soft elastic ball even with a very coarse mesh. The visual result is consistent with when finer resolution was used, demonstrating that our method allows a resolution-consistent simulation of volume preserving soft objects.

7.9 Squeezing Armadillo

To test the volume preservation and robustness of our method, we compress a 26K tet armadillo between two neighboring cylinders at the bottom and a moving cylinder at the top. The armadillo is divided into 6 zones: one for each arms and legs, the torso, and the entire body as a zone again. With Unconstrained Neo-Hookean $\nu = 0.495$, the armadillo loses up to 15.11% of its volume even with such a high Poisson ratio. When the top cylinder moves down enough to almost touch the bottom cylinders, the volume lost on the armadillo's body is not recovered and does not flow much outside of the region between the cylinders, and as a result the body of the armadillo is completely flattened. However, using our method with $\lambda = 60, \beta = 12$, we are able to preserve the volume of the armadillo completely. Notice the bulging around the edges of the armadillo's body, where the volume lost in the compressed areas are gathered. The visual difference in volume preservation can be seen in Figure 7.8 where the grid outlines the area the squeezed armadillo covers.

7.10 Leggings Fitting

We apply our method on a cloth fitting example as shown in Figure 7.9. The goal of this application is to predict fit of a tight fitting garment on a human subject. In this particular case a pair of leggings are fit onto a female subject. Because human flesh is largely volume preserving, our method is particularly suited for this example. We find that our method predicts a significantly different fit than an Unconstrained Neo-Hookean model with a large Poisson's ratio. This type of simulation is used to determine general aesthetic fit as well as comfort, which can be used to enhance the garment prototyping process.

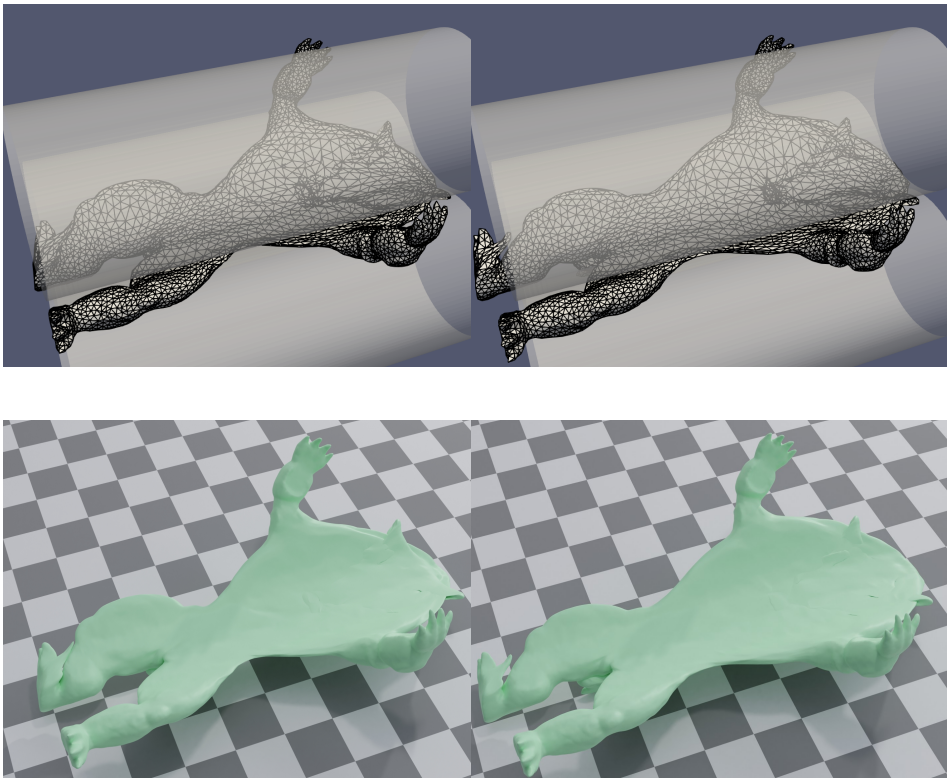

(a) UNH, $\nu = 0.495$ (b) Ours

Figure 7.8: Squeezing Armadillo: An armadillo is squeezed between three cylinders. Two cylinders are placed under the armadillo and the top cylinder is moved down to almost touch the bottom cylinders. (a) and (b) shows the results at the most extreme deformation, top row visualized with the cylinder and the mesh topology, and the bottom row rendered without the cylinder. Using UNH with $\nu = 0.495$, the armadillo loses 15.11% of its volume. Our method successfully preserves the entire volume of the armadillo, resulting in a much larger spread when completely deformed. The grid on the surface outlines the volume difference of the two deformed armadillos.

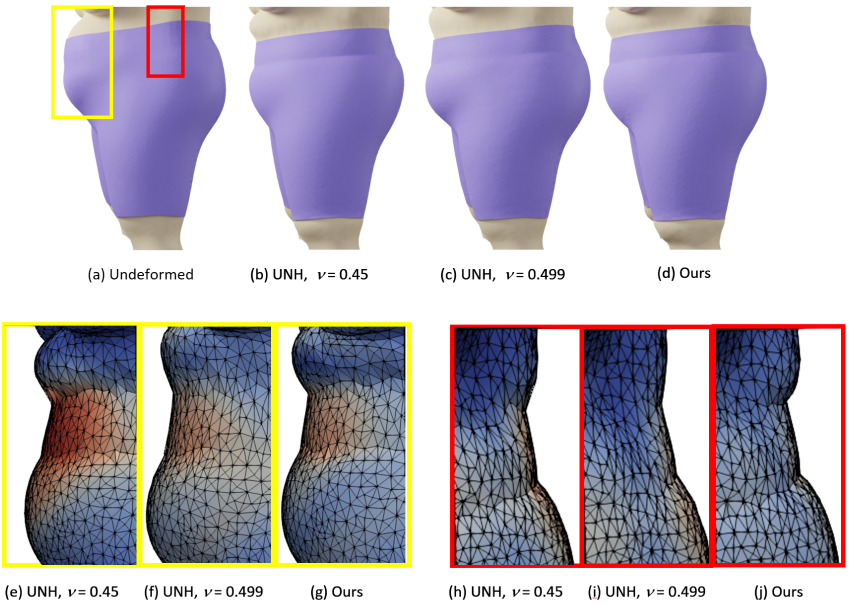

Figure 7.9: Leggigs fitting: Naively using $\nu = 0.4545$ produces qualitatively reasonable deformation, but the body loses a significant amount ($\sim$19%) of its volume, mostly in regions of high compression (see (b), and close-ups (e,h)). Using $\nu = 0.499$ preserves body volume up to an error of 0.5%, but produces limited deformations due to locking (c,f,i). By contrast, in our "Constrained Neo-Hookean" (CNH) method, we can designate volume preserving zones to match anatomical compartments, and exactly conserve volume within each zone while avoiding problems with volumetric locking. This results in more realistic displacement of soft tissues (d,g,j).

In addition to visual differences, volume preservation can lead to significant differences in the predictions of how well the garment fits; UNH with $\nu = 0.4545$ predicts a waistband circumference 7 cm smaller than that with $\nu = 0.499$, and 4.5cm smaller than with our method. Our results can improve predictions of human soft tissue mechanics in applications ranging from virtual try-ons to visual effects.

Example	Model	VC	λ	β	λ_e	t_r	$i_{\mathbf{avg}}$
Cloth-Body	SNH	no	400.0		0.0	12.10	21.32
Cloth-Body	SNH	no	40.0		0.0	12.93	23.09
Cloth-Body	Ours	yes	120.0	6.0	0.0	12.82	17.98
Cloth-Body	Ours	yes	120.0	6.0	100.0	14.63	19.18
Puck	SNH	no	40.0		0.0	1.55	3.00
Puck	SNH	no	400.0		0.0	1.58	3.14
Puck	Ours	yes	100.0	0.0	0.0	2.25	4.00
Puck	Ours	yes	100.0	9.0	0.0	1.93	3.38
Puck	Ours	yes	100.0	9.0	100.0	2.25	3.51
Suspend	SNH	no	400.0		0.0	1.02	7.28
Suspend	Ours	yes	40.0	0.0		1.02	6.52
Stretch	SNH	no	40.0		0.0	2.80	4.51
Stretch	SNH	no	400.0		0.0	9.91	14.33
Stretch	Ours	yes	25.0	0.0	0.0	7.89	9.92
Stretch	Ours	yes	25.0	1.0	0.0	7.28	9.24
Stretch	Ours	yes	25.0	1.0	10.0	6.25	7.33
Twist	SNH	no	100.0		0.0	86.06	138.33
Twist	Ours	no	100.0	9.0	0.0	37.32	50.33
Twist	Ours	yes	100.0	6.0	0.0	62.15	90.33
Twist	Ours	yes	100.0	6.0	15.0	103.10	92
Ball (Fine)	NH	no	120.0		0.0	17.27	14.64
Ball (Fine)	NH	no	400.0		0.0	19.00	15.90
Ball (Fine)	Ours	yes	120.0	1.0	0.0	17.91	12.29
Ball (Coarse)	NH	no	120.0		0.0	1.81	15.08
Ball (Coarse)	NH	no	400.0		0.0	2.50	21.84
Ball (Coarse)	Ours	yes	120.0	1.0	0.0	2.71	22.10
Armadillo	SNH	no	400.0		40.0	6.26	11.29
Armadillo	Ours	yes	60.0	12.0	40.0	6.97	10.84

Table 7.1: Performance Analysis: Performance table representing average run times per frame, and average Ipopt iterations per frame for major examples. SNH is the Stable Neo-Hookean [34]. (VC: Volume Constraint, t_r: Run Times per Frame (sec.), $i_{\mathbf{avg}}$: Avg. Ipopt Iterations.)

Chapter 8

Conclusion

Although our method generates more realistic volume preservation and reduces locking, for simulations without large deformations, the standard Neo-Hookean model may be sufficient due to its simplicity. This is especially true when no other constraints, such as due to external contact, are present in the simulation. Constrained optimization adds some complexity to the simulation, though our results in Table 7.1 show that the increase is computation times is not prohibitive in most cases. Overall, our findings allow a simple and inexpensive extension to existing FEM systems to solve the problem of volumetric locking while simulating incompressible materials such as the human body.

Performance Our formulation uses exact non-linear volume constraints on a non-linear optimization problem to preserve volume exactly in demanding applications like statics and dynamics with large time steps. This limits the choice of optimization solvers to ones that support non-linear equality constraints (e.g. Interior Point or SQP solvers). However, for dynamics problems with smaller time steps, or in applications with tolerance for volume loss/gain, we recommend linearizing the volume constraint, which drastically simplifies the problem. This can reduce the overhead of enforcing equality constraints, while still avoiding locking.

Choosing λ By decoupling λ from its physical meaning, our formulation is faced with an additional challenge, which is to determine how exactly λ effects the out-

come of a simulation. Fortunately, this is not a significant drawback since material parameters for standard Neo-Hookean FEM simulations also deviate from their measured values due to numerical stiffenning. This means that even the parameters of standard models require manual tuning to reproduce real phenomena in simulation. Luckily data-driven methods for determining simulation parameters (which has seen significant attention in recent literature) are generally agnostic to the true physical meaning of these parameters, and thus are equally as compatible with our method.

In conclusion, we presented a general method for realistic volumetric FEM simulations of human tissue. Our method provides exact volume preservation without the artificial stiffness due to volumetric locking using zonal volume constraints. This method gives artists the ability to define volume preserving zones that conform to anatomical compartments and automatically produces "squash-and-stretch" effects. In addition, we introduced an epidermis model for simulating skin dynamics, as an additional surface area-preserving potential. We also proposed a modification to the energy potential to provide control over local volume flow that results in improved recovery during extreme compression and inversion. Our approach can be applied to a variety of energy models. In particular, we have demonstrated the effectiveness of these simple modifications to the invariant based non-linear hyperelastic energies like the Neo-Hookean and Stable Neo-Hookean energy models.

Bibliography

[1] A. Angelidi, M. P. Canif, G. Wyvill, and S. King. Swirling-sweepers: constant-volume modeling. In *12th Pacific Conference on Computer Graphics and Applications, 2004. PG 2004. Proceedings.*, pages 10–15, Oct 2004. doi:10.1109/PCCGA.2004.1348329. → page 10

[2] D. N. Arnold, F. Brezzi, and M. Fortin. A stable finite element for the stokes equations. *Calcolo*, 21(4):337–344, 1984. → page 8

[3] I. Baran and J. Popović. Automatic rigging and animation of 3d characters. In *ACM Transactions on graphics (TOG)*, volume 26, page 72. ACM, 2007. → page 21

[4] K. Bathe. *Finite Element Procedures*. Prentice Hall, 2006. ISBN 9780979004902. URL https://books.google.ca/books?id=rWvefGICfO8C. → page 7

[5] K.-J. Bathe. The inf–sup condition and its evaluation for mixed finite element methods. *Computers & structures*, 79(2):243–252, 2001. → page 8

[6] J. Bonet and A. Burton. A simple average nodal pressure tetrahedral element for incompressible and nearly incompressible dynamic explicit applications. *Communications in Numerical Methods in Engineering*, 14(5):437–449, 1998. → pages 10, 27

[7] J. Bonet and R. D. Wood. *Nonlinear Continuum Mechanics for Finite Element Analysis, Cambridge University Press, Cambridge, UK*, volume 24. 03 2008. ISBN 978-0521838702. doi:10.1017/CBO9780511755446. → pages 6, 9

[8] D. Braess. *Finite elements: Theory, fast solvers, and applications in solid mechanics*. Cambridge University Press, 2007. → page 2

[9] O. Civit-Flores and A. Susín. Robust treatment of degenerate elements in interactive corotational fem simulations. In *Computer Graphics Forum*, volume 33, pages 298–309. Wiley Online Library, 2014. → page 9

[10] R. Diziol, J. Bender, and D. Bayer. Robust real-time deformation of incompressible surface meshes. pages 237–246, 08 2011. doi:10.1145/2019406.2019438. → page 10

[11] Y.-c. Fung. *Biomechanics: mechanical properties of living tissues*. Springer Science & Business Media, 2013. → page 1

[12] S. Hartmann and P. Neff. Polyconvexity of generalized polynomial-type hyperelastic strain energy functions for near-incompressibility. *International journal of solids and structures*, 40(11):2767–2791, 2003. → page 18

[13] G. Hirota, R. Maheshwari, and M. Lin. Fast volume-preserving free-form deformation using multi-level optimization. *Computer-Aided Design*, 32(8): 499 – 512, 2000. ISSN 0010-4485. doi:https://doi.org/10.1016/S0010-4485(00)00038-5. URL http://www.sciencedirect.com/science/article/pii/S0010448500000385. → page 10

[14] M. Hong, S. Jung, M. Choi, and S. W. J. Welch. Fast volume preservation for a mass-spring system. *IEEE Computer Graphics and Applications*, 26 (5):83–91, Sept 2006. ISSN 0272-1716. doi:10.1109/MCG.2006.104. → page 10

[15] G. Irving, J. Teran, and R. Fedkiw. Invertible finite elements for robust simulation of large deformation. In *Proceedings of the 2004 ACM SIGGRAPH/Eurographics Symposium on Computer Animation*, SCA '04, pages 131–140, Goslar Germany, Germany, 2004. Eurographics Association. ISBN 3-905673-14-2. doi:10.1145/1028523.1028541. URL https://doi.org/10.1145/1028523.1028541. → pages 11, 18

[16] G. Irving, C. Schroeder, and R. Fedkiw. Volume conserving finite element simulations of deformable models. *ACM Trans. Graph.*, 26(3), July 2007. ISSN 0730-0301. doi:10.1145/1276377.1276394. URL http://doi.acm.org/10.1145/1276377.1276394. → pages xii, 3, 8, 10, 14, 20, 27, 28, 29, 30

[17] A. Jacobson, I. Baran, L. Kavan, J. Popović, and O. Sorkine. Fast automatic skinning transformations. *ACM Transactions on Graphics (TOG)*, 31(4):77, 2012. → page 21

[18] D. L. James and C. D. Twigg. Skinning mesh animations. In *ACM Transactions on Graphics (TOG)*, volume 24, pages 399–407. ACM, 2005. → page 21

[19] P. Kaufmann. Discontinuous galerkin fem in computer graphics. 2012. → page 10

[20] R. Kikuuwe, H. Tabuchi, and M. Yamamoto. An edge-based computationally efficient formulation of saint venant-kirchhoff tetrahedral finite elements. *ACM Transactions on Graphics (TOG)*, 28(1):8, 2009. → pages x, 19

[21] T. Liu, S. Bouaziz, and L. Kavan. Quasi-newton methods for real-time simulation of hyperelastic materials. *ACM Trans. Graph.*, 36(3), May 2017. ISSN 0730-0301. doi:10.1145/2990496. URL http://doi.acm.org/10.1145/2990496. → page 9

[22] I. Macêdo, J. P. Gois, and L. Velho. Hermite interpolation of implicit surfaces with radial basis functions. In *2009 XXII Brazilian Symposium on Computer Graphics and Image Processing*, pages 1–8. IEEE, 2009. → page 21

[23] A. McAdams, Y. Zhu, A. Selle, M. Empey, R. Tamstorf, J. Teran, and E. Sifakis. Efficient elasticity for character skinning with contact and collisions. *ACM Trans. Graph.*, 30(4):37:1–37:12, July 2011. ISSN 0730-0301. doi:10.1145/2010324.1964932. URL http://doi.acm.org/10.1145/2010324.1964932. → pages 6, 9

[24] M. Mooney. A theory of large elastic deformation. *Journal of applied physics*, 11(9):582–592, 1940. → page 9

[25] M. Müller, J. Dorsey, L. McMillan, R. Jagnow, and B. Cutler. Stable real-time deformations. In *Proceedings of the 2002 ACM SIGGRAPH/Eurographics Symposium on Computer Animation*, SCA '02, pages 49–54, New York, NY, USA, 2002. ACM. ISBN 1-58113-573-4. doi:10.1145/545261.545269. URL http://doi.acm.org/10.1145/545261.545269. → page 9

[26] E. D. S. Neto, F. A. Pires, and D. Owen. F-bar-based linear triangles and tetrahedra for finite strain analysis of nearly incompressible solids. part i: formulation and benchmarking. *International Journal for Numerical Methods in Engineering*, 62(3):353–383, 2005. → page 15

[27] D. K. Pai, A. Rothwell, P. Wyder-Hodge, A. Wick, Y. Fan, E. Larionov, D. Harrison, D. R. Neog, and C. Shing. The human touch: Measuring contact with real human soft tissues. *ACM Trans. Graph.*, 37(4):58:1–58:12, July 2018. ISSN 0730-0301. doi:10.1145/3197517.3201296. URL http://doi.acm.org/10.1145/3197517.3201296. → pages 21, 31

[28] E. Promayon, P. Baconnier, and C. Puech. Physically based deformations constrained in displacements and volume. *Computer Graphics Forum (Proc. of Eurographics '96)*, 15, 08 1996. doi:10.1111/1467-8659.1530155. → page 10

[29] M. Puso and J. Solberg. A stabilized nodally integrated tetrahedral. *International Journal for Numerical Methods in Engineering*, 67(6): 841–867, 2006. → page 8

[30] R. S. Rivlin and E. K. Rideal. Large elastic deformations of isotropic materials iv. further developments of the general theory. *Philosophical Transactions of the Royal Society of London. Series A, Mathematical and Physical Sciences*, 241(835):379–397, 1948. doi:10.1098/rsta.1948.0024. URL https://royalsocietypublishing.org/doi/abs/10.1098/rsta.1948.0024. → pages 9, 16

[31] D. Rohmer, S. Hahmann, and M.-P. Cani. Exact volume preserving skinning with shape control. In *Proceedings of the 2009 ACM SIGGRAPH/Eurographics Symposium on Computer Animation*, SCA '09, pages 83–92, New York, NY, USA, 2009. ACM. ISBN 978-1-60558-610-6. doi:10.1145/1599470.1599481. URL http://doi.acm.org/10.1145/1599470.1599481. → pages 10, 21

[32] G. Scovazzi, B. Carnes, X. Zeng, and S. Rossi. A simple, stable, and accurate linear tetrahedral finite element for transient, nearly, and fully incompressible solid dynamics: a dynamic variational multiscale approach. *International Journal for Numerical Methods in Engineering*, 106(10): 799–839, 2016. → page 8

[33] E. Sifakis and J. Barbic. Fem simulation of 3d deformable solids: A practitioner's guide to theory, discretization and model reduction. In *ACM SIGGRAPH 2012 Courses*, SIGGRAPH '12, pages 20:1–20:50, New York, NY, USA, 2012. ACM. ISBN 978-1-4503-1678-1. doi:10.1145/2343483.2343501. URL http://doi.acm.org/10.1145/2343483.2343501. → page 9

[34] B. Smith, F. D. Goes, and T. Kim. Stable neo-hookean flesh simulation. *ACM Trans. Graph.*, 37(2):12:1–12:15, Mar. 2018. ISSN 0730-0301. doi:10.1145/3180491. URL http://doi.acm.org/10.1145/3180491. → pages viii, x, 3, 9, 10, 11, 18, 19, 38

[35] A. Stomakhin, R. Howes, C. Schroeder, and J. M. Teran. Energetically consistent invertible elasticity. In *Proceedings of the 11th ACM SIGGRAPH / Eurographics Conference on Computer Animation*, EUROSCA'12, pages 25–32, Aire-la-Ville, Switzerland, Switzerland, 2012. Eurographics Association. ISBN 978-3-905674-37-8. doi:10.2312/SCA/SCA12/025-032. URL http://dx.doi.org/10.2312/SCA/SCA12/025-032. → pages 3, 11, 15

[36] T. Sussman and K.-J. Bathe. A finite element formulation for nonlinear incompressible elastic and inelastic analysis. *Computers & Structures*, 26 (1-2):357–409, 1987. → page 7

[37] J. Teran, E. Sifakis, G. Irving, and R. Fedkiw. Robust quasistatic finite elements and flesh simulation. In *Proceedings of the 2005 ACM SIGGRAPH/Eurographics Symposium on Computer Animation*, SCA '05, pages 181–190, New York, NY, USA, 2005. ACM. ISBN 1-59593-198-8. doi:10.1145/1073368.1073394. URL http://doi.acm.org/10.1145/1073368.1073394. → page 11

[38] W. v. Funck, H. Theisel, and H. Seidel. Explicit control of vector field based shape deformations. In *15th Pacific Conference on Computer Graphics and Applications (PG'07)*, pages 291–300, Oct 2007. doi:10.1109/PG.2007.26. → page 10

[39] R. Vaillant, L. Barthe, G. Guennebaud, M.-P. Cani, D. Rohmer, B. Wyvill, O. Gourmel, and M. Paulin. Implicit skinning: real-time skin deformation with contact modeling. *ACM Transactions on Graphics (TOG)*, 32(4):125, 2013. → page 21

[40] A. Wächter and L. T. Biegler. On the implementation of an interior-point filter line-search algorithm for large-scale nonlinear programming. *Mathematical Programming*, 106(1):25–57, Mar 2006. ISSN 1436-4646. doi:10.1007/s10107-004-0559-y. URL https://doi.org/10.1007/s10107-004-0559-y. → page 23

[41] H. Wang and Y. Yang. Descent methods for elastic body simulation on the gpu. *ACM Transactions on Graphics (TOG)*, 35(6):1–10, 2016. → page 11

[42] O. Weber, O. Sorkine, Y. Lipman, and C. Gotsman. Context-aware skeletal shape deformation. In *Computer Graphics Forum*, volume 26, pages 265–274. Wiley Online Library, 2007. → page 21

[43] H. Wendland. *Scattered data approximation*, volume 17. Cambridge university press, 2004. → page 21

[44] S.-H. Yoon and M.-S. Kim. Sweep-based freeform deformations. *Comput. Graph. Forum*, 25:487–496, 09 2006. doi:10.1111/j.1467-8659.2006.00968.x. → page 10

Appendix A

Appendix

Extending the idea of (5.1), one can devise a more highly nonlinear versions of the penalty functional. For example, from

$$\frac{\partial^2 U_2(J;\beta)}{\partial J^2} = \beta(J-1)^4 + 1, \tag{A.1}$$

we can derive

$$\frac{\partial U_2(J;\beta)}{\partial J} = \frac{1}{5}(J-1)\left[\beta(J-1)^4 + 5\right], and \tag{A.2}$$

$$U_2(J;\beta) = \frac{1}{30}(J-1)^2\left[\beta(J-1)^4 + 15\right]. \tag{A.3}$$

In this sense, we can derive a penalty function of arbitrary order, based on the second derivative. To satisfy condition **e** from Section 5, the order of the second derivative must be an even number, so for a natural number n one can define a second derivative as

$$\frac{\partial^2 U_n(J;\beta)}{\partial J^2} = \beta(J-1)^{2n} + 1, \tag{A.4}$$

then build the penalty function $U_n(J;\beta)$ that satisfies all the five conditions from the second derivative as follows,

$$U_n(J;\beta) = \frac{1}{(2n+1)(2n+2)}(J-1)^2\left[\beta(J-1)^{2n} + \frac{(2n+1)(2n+2)}{2}\right]. \tag{A.5}$$

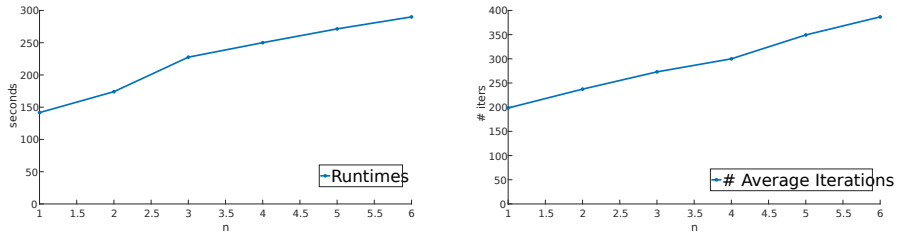

(a) (b)

Figure A.1: Penalty Function Performance: A plot of penalty functions U_n of different orders n from 1 to 6.

We plot the runtimes and average Ipopt iterations for the first few n of these penalties, for the cube twist simulation in Figure A.1, with $\beta = 1$. Notice how the runtime and number of iterations increase linearly depending on n. From this simple experiment, we can conclude that although the added nonlinearity of the gradient is beneficial for resolving tet inversions, additional nonlinearity of the energy is actually harmful for the performance. Therefore, we argue that our choice of the penalty functional in (5.1) is indeed optimal for our purposes.